Research Article

Label-Free Detection of Human Serum Using Surface-Enhanced Raman Spectroscopy Based on Highly Branched Gold Nanoparticle Substrates for Discrimination of Non-Small Cell Lung Cancer

Xiaowei Cao [1,2,3] **Zhenyu Wang,** [1,4] **Liyan Bi,** [5] **and Jie Zheng** [3]

[1]*Institute of Translational Medicine, Medical College, Yangzhou University, Yangzhou 225001, China*
[2]*Jiangsu Co-Innovation Center for Prevention and Control of Important Animal Infectious Diseases and Zoonoses, Yangzhou University, Yangzhou 225009, China*
[3]*Intensive Care Unit, Wuxi Third People's Hospital, Wuxi 214000, China*
[4]*Jiangsu Key Laboratory of Experimental & Translational Non-Coding RNA Research, Medical College, Yangzhou University, Yangzhou 225001, China*
[5]*Transformative Otology and Neuroscience Center, College of Special Education, Binzhou Medical University, Yantai 264003, China*

Correspondence should be addressed to Xiaowei Cao; cxw19861121@163.com

Surface-enhanced Raman spectroscopy (SERS) is a good candidate for the development of fast and easy-to-use diagnostic tools, possibly used on serum in screening tests. In this study, a potential label-free serum test based on SERS spectroscopy was developed to analyze human serum for the diagnosis of the non-small cell lung cancer (NSCLC). We firstly synthesized novel highly branched gold nanoparticles (HGNPs) at high yield through a one-step reduction of $HAuCl_4$ with dopamine hydrochloride at 60°C. Then, HGNP substrates with good reproducibility, uniformity, and high SERS effect were fabricated by the electrostatically assisted (3-aminopropyl) triethoxysilane-(APTES-) functionalized silicon wafer surface-sedimentary self-assembly method. Using as-prepared HGNP substrates as a high-performance sensing platform, SERS spectral data of serum obtained from healthy subjects, lung adenocarcinoma patients, lung squamous carcinoma patients, and large cell lung cancer patients were collected. The difference spectra among different types of NSCLC were compared, and analysis result revealed their intrinsic difference in types and contents of nucleic acids, proteins, carbohydrates, amino acids, and lipids. SERS spectra were analyzed by principal component analysis (PCA), which was able to distinguish different types of NSCLC. Considering its time efficiency, being label-free, and sensitivity, SERS based on HGNP substrates is very promising for mass screening NSCLC and plays an important role in the detection and prevention of other diseases.

1. Introduction

Lung cancer is presently the most commonly diagnosed metastatic tumor and a leading cause of cancer-related deaths in the world. Approximately 85% of lung cancers are non-small cell lung cancer (NSCLC), which mainly includes lung adenocarcinoma, lung squamous carcinoma, and large cell lung cancer [1, 2]. The high mortality is mainly due to its aggressiveness, and the fact is that most NSCLC are generally detected at the late stage of inoperable disease. Early detection of NSCLC can dramatically improve the outcome of fatal disease. NSCLC has no visible symptoms at the early stages, and the widespread medical screening is serving as a significant modality for early detection of NSCLC. For the best use of public health resources, it is extremely important to diagnose as much histological type

of NSCLC as possible in every population-based cancer screening program [3]. At present, several conventional methods involving clinical examination, white light endoscopy, and histopathological analysis are not only costly, time-consuming, and invasive, but also require sophisticated instruments [4]. These drawbacks hindered the further clinical application in the diagnosis and discrimination of cancer. Therefore, developing novel diagnosis methods for NSCLC is essential.

Surface-enhanced Raman scattering (SERS) is a vibrational spectroscopy technique based on the intensity amplification of Raman scattering by metallic nanostructures with suitable plasmonic characteristics [5]. SERS can reflect the molecular structures and changes of samples and is considered as the molecular "fingerprint" [5]. Compared with other techniques, SERS has advantages such as being noninvasive, high spatial resolution, weak water scattering, and no sample preparation [6, 7]. In addition, Raman scattering can be enhanced by as much as 6 to 14 orders of magnitude when the analyses are adsorbed onto the roughened surfaces of the metallic nanostructure [8]. So, it is very suitable for studying biological sample containing water. Because of extremely rich biochemical and biological information of biofluids, SERS spectral analysis of biofluids for diagnosis and screening of disease may provide a feasible way for cancer diagnosis. Attempts were made to identify cancer-related chemical and bimolecular changes in urine, serum, cervical fluid, plasma, and saliva using this technique [9–11]. Li et al. investigated the use of SERS spectra of serum samples from healthy individuals, atrophic gastritis patients, pre- and postoperation gastric cancer patients to diagnose gastric diseases. Their experiment results demonstrated that spectroscopy can effectively record the changes occurring in serum caused by variations in body circumstances [12]. González-Solís et al. discriminated the serum obtained from three types of leukemia patients by using Raman spectroscopy, and the possibility for distinguishing different types of cancer by this technique has been preliminarily demonstrated [13].

SERS effect of nanomaterials is extremely important when detecting biofluids in which some components were rare. Nanomaterials with different sizes, shapes, and compositions have been prepared for SERS detection [14]. Recently, highly branched gold nanoparticles (HGNPs) with a central core and external multiple sharp tips have received a great deal of attention for its unique optical properties. The optical properties of HGNPs may be controlled by changing the size, shape, and number and length of sharp branches. It demonstrated that HGNPs have higher sensitivity in localized surface plasmon resonance (LSPR) as compared with other nanoparticles [15, 16]. HGNPs have a roughened surface determined by many branches and cavities, which act as potential "hot spots" for enhancing the electromagnetic field around the nanoparticle [17]. Due to its excellent SERS effect, SERS based on HGNPs has been applied to the biomolecular detection, medical imaging, and diagnosis of various cancers [18, 19]. In order to get greater sensitivity and signal enhancement, a variety of nanoparticles have been

assembled into solid substrates (such as graphite, silicon, and ITO glass) by template method, self-assembly, and electrochemical deposition. Rodrı́guez-Lorenzo et al. reported that a uniform and reproducible gold nanostars substrate could generate a high enhancement factor (EF) when using 1,5-naphtalenedithiol as an analyte [20]. According to the calculations performed by Indrasekara et al. SERS EF of gold nanostars substrate could approach 9 orders of magnitude, which was attributed to the high efficacy coupled "hot spots" produced between the nanoparticles and the dielectric silicon substrate [21].

In this study, SERS spectroscopy based on highly branched gold nanoparticle (HGNP) substrate was used to investigate the spectral characteristics of human serum for the purpose of diagnosing NSCLC (Scheme 1). Firstly, a one-step method for synthesizing novel anisotropic HGNPs with multiple tips and dendritic structures was proposed by using dopamine. Briefly, HGNPs were synthesized by combining $HAuCl_4$ with dopamine hydrochloride in a rapid one-step reaction. Then, HGNPs were assembled onto the surface of (3-aminopropyl) triethoxysilane- (APTES-) functionalized silicon wafer by the sedimentary self-assembly method. The SERS stability, homogeneity, and sensitivity of HGNP substrates were evaluated. Subsequently, we utilized the as-prepared HGNPs substrates to detect the SERS spectra of serum from healthy subjects and three types of NSCLC (lung adenocarcinoma, lung squamous carcinoma, and large cell lung cancer). The difference spectra were employed to identify the differences of biochemical components among different groups. In addition, SERS spectra were analyzed by using principal component analysis (PCA), demonstrating that SERS spectroscopy was a sensitive analysis technology for classification and discrimination of the different types of NSCLC.

2. Materials and Methods

2.1. Materials. Ultrapure water from Milli-Q (Millipore, USA, resistivity >18 M) was used throughout the experiments. Chloroauric acid tetrahydrate ($HAuCl_4·4H_2O$) and dopamine hydrochloride were all purchased from Yangzhou Younuo Chemicals Co., Ltd. (China). The (3-aminopropyl) triethoxysilane (APTES) was purchased from Yangzhou Noah Chemical Co., Ltd. (China). All glassware used was cleaned with aqua regia and ultrapure water.

2.2. Collection and Storage of Serum Samples. Blood samples were drawn from donors who signed an informed consent form in accordance with the ethical guidelines published by the Council for International Organizations of Medical Sciences. This study was approved by the Medical College of Yangzhou University and followed the guidelines of the Helsinki Declaration. There were 30 health subjects, 30 lung adenocarcinoma patients, 30 lung squamous carcinoma patients, and 30 large cell lung cancer patients. All patient specimens were obtained from Clinical Medical Colleges of Yangzhou University. The health subjects samples were collected from volunteers at Yangzhou University. The
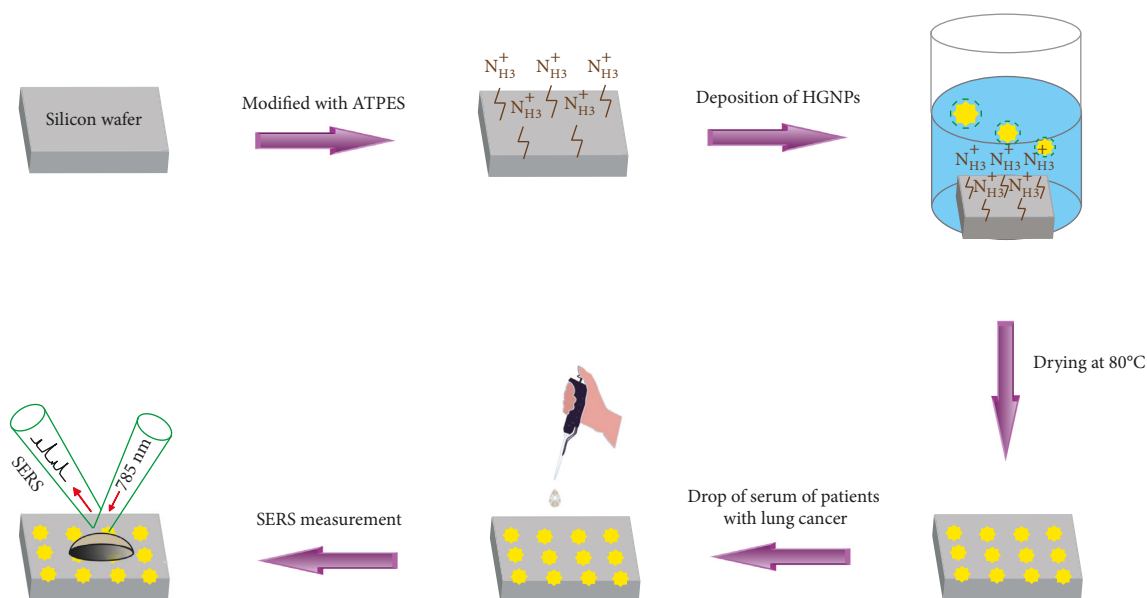
SCHEME 1: Illustration of the fabrication procedure of the HGNP substrate and SERS is used for diagnosis and discrimination of the NSCLC.

detailed information of study population (e.g., age, gender, and histopathological stage) is summarized in Table 1. Each blood sample was approximately 5 mL in volume and was extracted intravenously from volunteers before breakfast to avoid the interference of food. Then, the blood sample was deposited at 4°C for 4 h and was centrifuged at 3000 rpm for 10 min in order to remove the blood cells, fibrinogen, and platelets. After the centrifugation, the serum was obtained and stored at −80°C for SERS measurement.

2.3. Preparation of Highly Branched Gold Nanoparticles.
For the preparation of HGNPs, 0.4 mL HAuCl$_4$ solution (25 mM) was mixed with 10 mL of ultrapure water under vigorous stirring. Then, 2 mL dopamine hydrochloride solution (53 mM) was added. The mixed solution was heated slowly until the temperature reached 60°C. The temperature was fixed at 60°C and we let it continue to react for about 30 minutes to synthesize HGNPs.

2.4. Assembly of HGNPs on APTES-Functionalized Silicon Wafer.
The fabrication of HGNPs substrates is displayed in Scheme 1. The silicon wafer was washed with aqua regia and rinsed with ultrapure water for three times. The wafer was further cleaned in ethanol for three times and dried at 80°C for 2 h in an air oven. After drying, the silicon wafer was immersed in 1% (v/v) APTES of anhydrous ethanol for 24 h to form a self-assembled layer followed by thorough rinsing with ethanol and air drying. Subsequently, the APTES-functionalized silicon wafer was placed horizontally in the HGNP colloidal solution for 12 h. HGNPs were deposited onto the surfaces of the APTES-functionalized silicon wafer to obtain the HGNP layer. The thiol moiety of APTES covalently binds to the substrate while its pendant primary amine group covalently binds to the nanoparticles. Thus, the HGNP substrates were obtained.

TABLE 1: Demographics of study population.

Groups	Healthy subjects ($n = 30$)	Lung adenocarcinoma ($n = 30$)	Lung squamous carcinoma ($n = 30$)	Large cell lung cancer ($n = 30$)
Age (years)				
Mean	25	56	48	50
Gender (%)				
Male	16	15	13	15
Female	14	15	17	15
Cancer stage				
I-II		12	10	13
III-IV		18	20	17

2.5. SERS Measurement.
SERS spectral data was collected from an inverted microscope (Renishaw) in the 600–1800 cm^{-1} range with a 785-nm He-Ne laser maintained. The laser intensity was 5 mW and the exposure time was 10 s. The laser was focused onto the sample using a 50× long working distance objective. For SERS measurement of human serum, 100 mL serum sample obtained from each volunteer participating in this study was dropped directly on the HGNPs substrate, and then detected 10 times by Raman spectroscopy to obtain their own fingerprints. Subsequently, the measured SERS spectra of 30 volunteers were used to obtain an average SERS spectrum of serum for each histological type of NSCLC.

2.6. Characterization.
The ultraviolet-visible-near infrared (UV-vis-NIR) absorption spectrum was measured using a Cary UV-5000 spectrometer (Agilent). Transmission electron microscope (TEM) imaging was performed using a Tecnai 12 transmission electron microscope operating at

an accelerating voltage of 60 kV (Philips). Scanning electron microscopy (SEM) images were acquired using a S-4800 II field-emission scanning electron microscope (FESEM) operating at 3.0 kV (Hitachi). To observe the crystalline structure of the particles, high-resolution TEM images (HRTEM) and selected area electron diffraction (SAED) images were captured by a Tecnai G2 F30 S-Twin TEM at 200 KV (FEI).

3. Results and Discussion

3.1. Characterization of HGNPs. The morphology and structure of the HGNPs were characterized using SEM and TEM. As shown in Figure 1(a), HGNPs were well dispersed with particle sizes of ~600 nm and these nanoparticles exhibited multiple tips with dendritic structures. The high-magnification SEM image and TEM image further revealed that each HGNP consisted of a solid gold core with many sharp, irregular tips (Figures 1(b) and 1(c)). The crystalline structure of the HGNPs was observed by HRTEM. Figure 1(d) reveals that the interplanar spacing of the tips was measured to be 0.24 nm, indicating that the HGNPs grew preferentially on {111} planes. To further understand the crystal structure of HGNPs, a SAED image was also taken (Figure 1(e)). HGNPs grow in random orientations like {111}, {200}, {220}, and {311} crystalline facet. The results indicated that as-prepared HGNPs were pure and well crystallized gold. Figure 1(f) shows that the UV-vis-NIR absorption spectrum of HGNPs had a strong absorption peak at 475 nm. During the reaction process, the color of the solution turned from light yellow to dark green and finally to orange-red within 30 minutes. Therefore, HGNPs were synthesized using this simple, fast, and large-scale method.

Besides, Raman spectra of 4-MBA and 4-MBA labeled HGNPs are recorded in Figure 1(g). 4-MBA was chosen as an analyte, which had two SERS characteristic peaks at 1080 cm^{-1} and 1587 cm^{-1} [22]. We observed the strong SERS signals from 4-MBA-labeled HGNPs, indicating that HGNPs had a strong surface enhancement effect. The significant enhancement might be due to the large amount of sharp tips on the surface of HGNPs that potentially act as "hot spots." Besides, the enhancement factor (EF) of HGNPs was calculated by using the expression EF = $(I_{SERS}/C_{SERS})/(I_{RS}/C_{RS})$, where I_{SERS} corresponds to the SERS intensity obtained for the HGNPs colloidal dispersion at a certain concentration C_{SERS} of the analyte, and I_{RS} corresponds to the Raman intensity obtained under non-SERS conditions at an analyte concentration C_{RS}. During the experimental process, the HGNP colloid was mixed with the same volume of 4-MBA solution (2×10^{-5} M) for 4 h, giving a final concentration with 10^{-5} M. When C_{SERS} was 1×10^{-5} M and C_{RS} was 1×10^{-2} M, EF was calculated to be 5.7×10^{5}, which was higher than the gold nanostars (2×10^{5}) reported by Nalbant Esenturk [23].

3.2. Fabrication of HGNPs Substrates. HGNP substrates were fabricated by the electrostatic self-assembly method,

which does not need complicated equipment and is preponderant in commercial manufacture. The aminosilane groups of APTES can boost the adsorption of nanoparticles with inherent negative charge, so it was employed to functionalize the silicon wafers assisted by electrostatic interaction for adsorption of HGNPs layers [24]. Here, HGNPs were successful in depositing and adsorbing on the surface of the APTES-functionalized silicon wafer by directly placing the wafers horizontally into the HGNPs colloidal dispersion. Figure 2(a) shows the SEM image of the HGNP substrate. HGNPs had slight aggregation and uniformly distribution on the surface of silicon wafer. To characterize the uniformity of the surface SERS signal, a SERS mapping experiment was carried out after the surface was adsorbed with 4-MBA (1×10^{-5} M). The scan area was 25×25 mm^2, the step size was $2\,\mu$m, the laser power was 5 mW, and the acquisition time at each point was 10 s. The SERS intensity of the 1080-cm^{-1} peak was mapped at each grid point on the substrate. As shown in Figure 2(b), SERS mapping was used to display the intensity of the 1080-cm^{-1} characteristic peak at each grid point according to a color scheme ranging from blue (lowest intensity) through green, yellow, orange, and red (highest intensity). The color of SERS mapping is basically the same, indicating that the HGNP substrate has a very uniform SERS enhancement effect over the whole surface, although some aggregates can still be found at some spots.

We further investigated the stability of the SERS signals of 4-MBA-labeled HGNP substrates. HGNPs substrates were stored for several days at room temperature and the corresponding SERS spectra were measured (Figure 3(a)). After 15 days, compared with the freshly prepared substrates, SERS intensity of the characteristic peak at 1080 cm^{-1} was reduced by only 8.7% in Figure 3(b). The result showed that the substrates displayed a very stable SERS enhancement effect. In order to study the detection capability of the substrates, 4-MBA at different concentrations were introduced to the HGNP substrates. Figure 3(c) shows the SERS spectra of 4-MBA at different concentrations absorbed on the HGNP substrates. The lower concentration of 4-MBA solutions showed a silence of SERS signal, and thus the 5×10^{-10} M concentration was taken as the limit of detection (LOD) for the 4-MBA. The relationship between the intensity of characteristic peak at 1080 cm^{-1} and the concentration of 4-MBA solution was analyzed (Figure 3(d)). The SERS intensities at 1080 cm^{-1} increased constantly with the increase of 4-MBA concentration. Raman intensity of 4-MBA solution at low concentrations (from 5×10^{-10} to 1×10^{-9} M) did not change significantly, which may be caused by the systematic error during the experiment. There were linear relationships between the peak intensity at 1080 cm^{-1} and the concentrations of the 4-MBA solution from 1×10^{-8} M to 1×10^{-4} M. Its regression equation can be expressed as $y = 15658 \lg C + 133289$ (C being the concentration of the 4-MBA). Therefore, by careful assessment of the calibration curve, we got LOD and limits of quantification (LOQ) of 5×10^{-10} M and 1×10^{-8} M, respectively. Besides the stability and sensitivity, reproducibility of the substrates was another important factor for SERS detection.
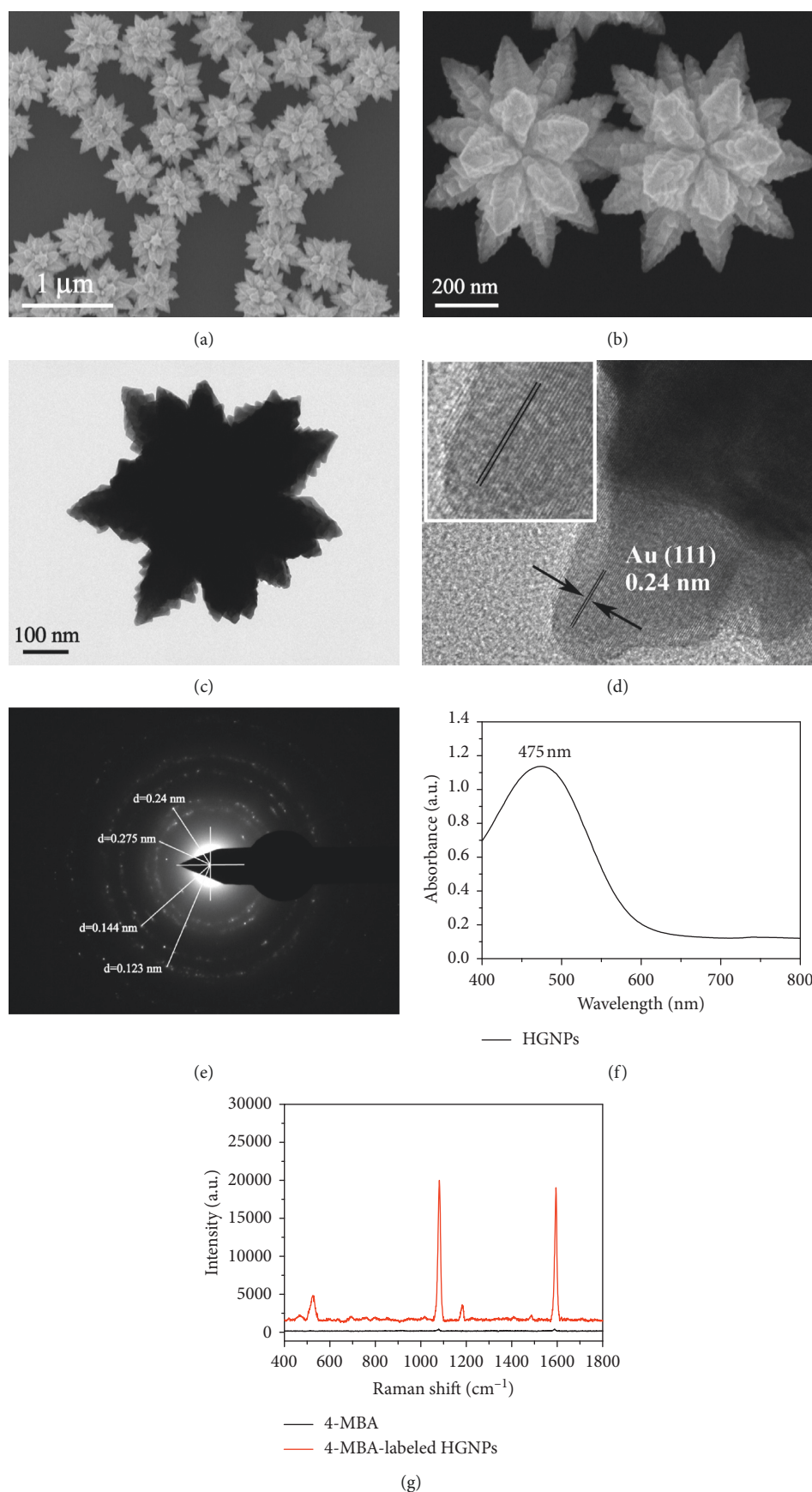
(a)

(b)

(c)

(d)

(e)

(f)

(g)

FIGURE 1: (a) Low and (b) high magnification SEM images of the HGNPs. (c) TEM images and (d) high-resolution TEM images of the HGNPs. (e) SAED pattern and (f) UV-vis-NIR absorption spectrum of the HGNPs. (g) SERS spectra of (black curve) 4-MBA and (red curve) HGNP colloidal dispersion mixed with 4-MBA under 785 nm excitation.
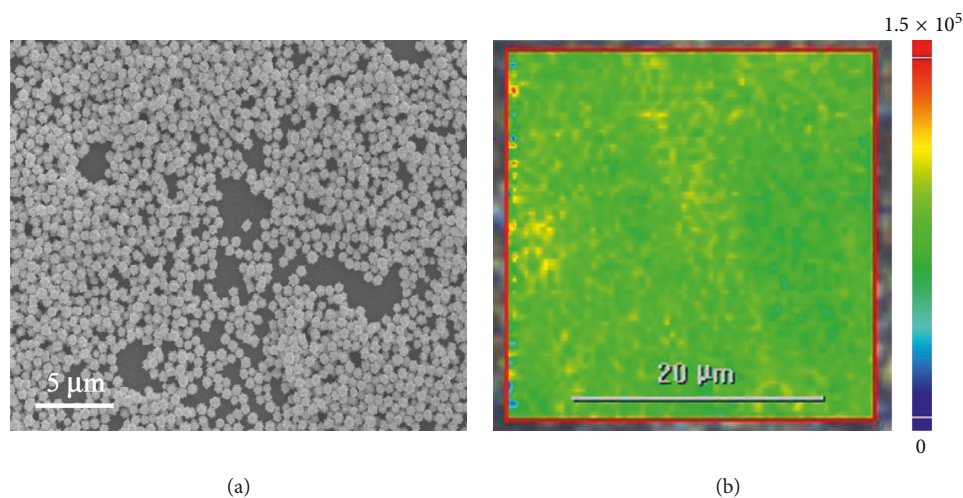
(a)

(b)

FIGURE 2: (a) SEM images of the HGNPs substrate. (b) SERS mapping of 4-MBA measured at $1080\,\text{cm}^{-1}$ using the HGNP substrate. The acquisition time was $10\,\text{s}$, and the laser power was $5\,\text{mW}$.

(a)

(b)

(c)

(d)

FIGURE 3: Continued.

(e)

(f)

—— Clean HGNPs substrate

(g)
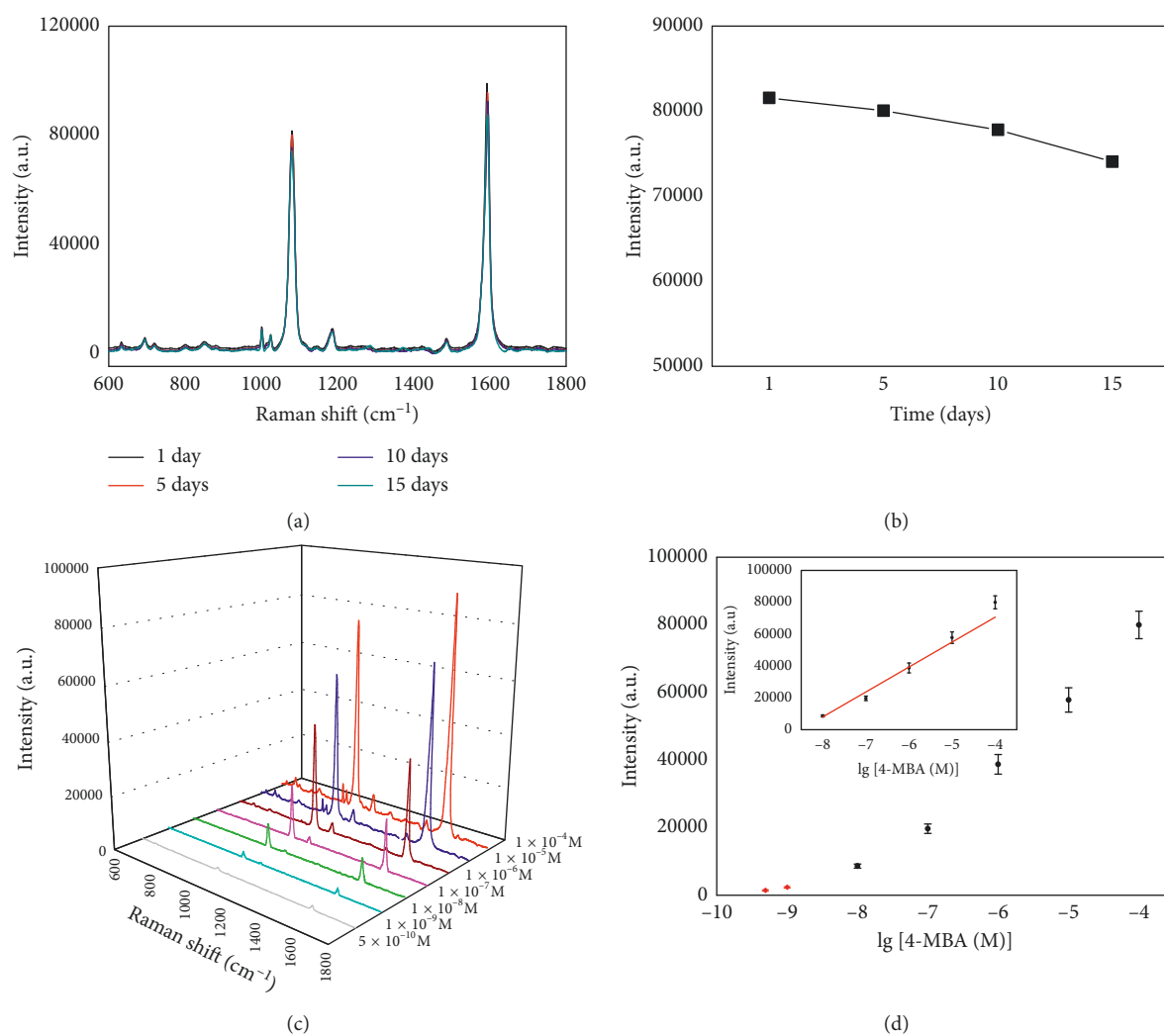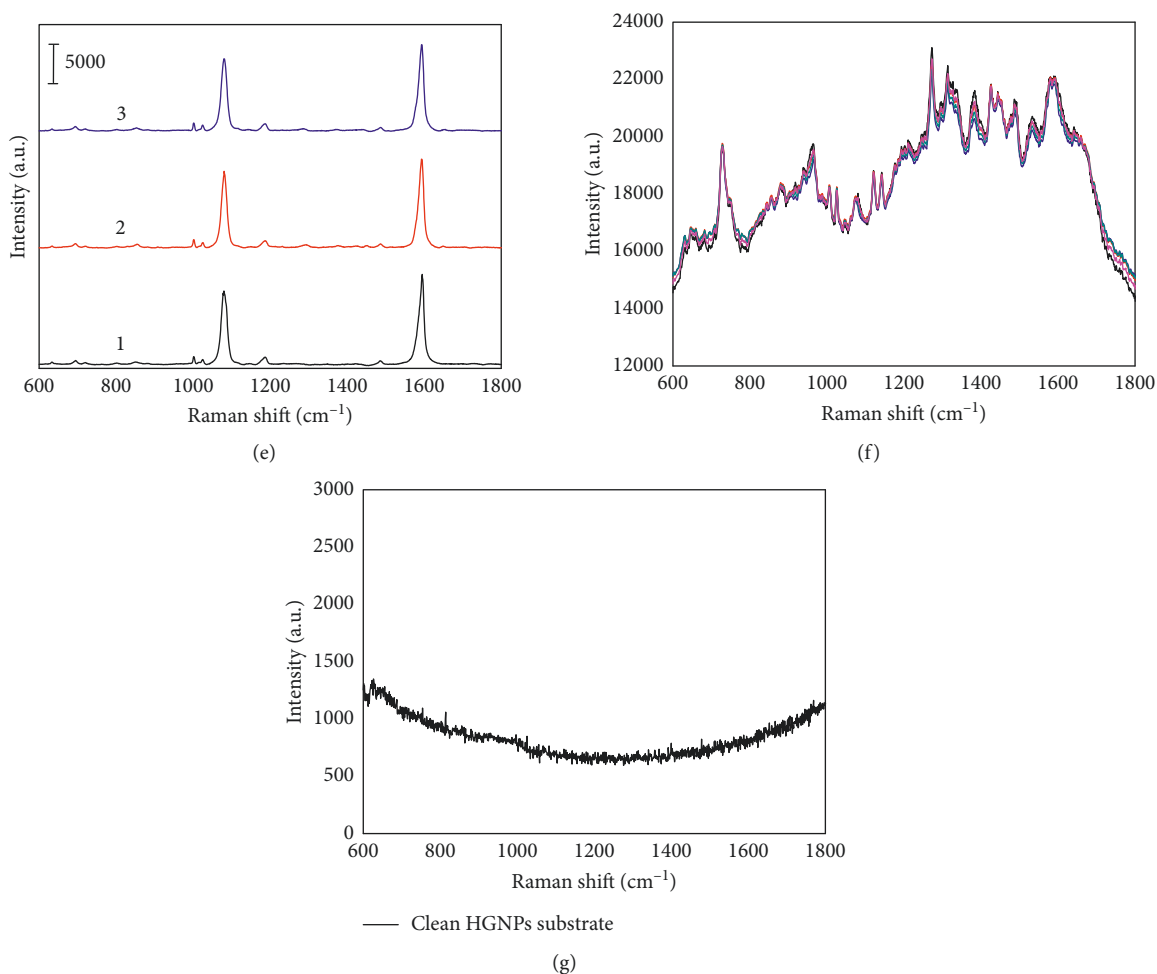
FIGURE 3: (a) SERS stability of HGNP substrates measured with 4-MBA (1×10^{-4} M). 4-MBA-labeled HGNP substrates were stored for several days at room temperature. (b) SERS intensities of the bands at 1080 cm^{-1} corresponding to the SERS spectra in (a). (c) SERS spectra of 4-MBA at different concentrations (5×10^{-10}, 1×10^{-9}, 1×10^{-8}, 1×10^{-7}, 1×10^{-6}, 1×10^{-5}, and 1×10^{-4} M) absorbed on the HGNP substrates. (d) The Raman intensity of 4-MBA at 1080 cm^{-1} as a function of the concentration of 4-MBA. The inset is the calibration curve of 4-MBA at the concentration from 1×10^{-8} to 1×10^{-4} M. (e) The reproducibility of HGNP substrates measured with 4-MBA (1×10^{-4} M). (f) The repeatability of the SERS spectrum of serum on the substrate. (g) SERS spectra of unlabeled HGNP substrates.

Three substrates, made at different times, were measured and are shown in Figure 3(e). The deviation of peak height at 1080 cm^{-1} was 6.4%, which supported the good reproducibility of the SERS substrates. In order to evaluate the repeatability of the SERS spectrum of serum on the substrate, the serum sample from the same large cell lung cancer patient was dropped directly onto the surfaces of five different HGNP substrates, and then subjected to Raman spectroscopy. Figure 3(f) shows the repeatability of the SERS spectrum of serum on the substrate. These SERS spectra looked very similar, and there were no obvious differences in characteristic peak positions and peak intensities. It demonstrated that HGNP substrates with good reproducibility were very suitable for serum SERS label-free detection. In Figure 3(g), the unlabeled HGNP substrates had no obvious characteristic peaks, and it suggested that the substrates had a clean background in the SERS spectrum. Taken together, the clean HGNP substrates with ultrahigh sensitivity, homogeneous SERS activity, and high reproducibility are

prepared and can be used as a promising candidate for label-free detection of biological samples.

3.3. SERS Spectroscopy of Human Serum. As a label-free detection method, the serum was dropped directly on the HGNP substrate to obtain the rich molecular and structural information. The SERS spectrum of serum for each type of NSCLC was obtained by averaging 30 subjects. Figure 4 shows the average SERS spectra of serum obtained from large cell lung cancer patients, lung adenocarcinoma patients, lung squamous carcinoma patients, and healthy subjects. There are many characteristic vibrational bands which may be attributed to proteins, nucleic acids, lipids, and carbohydrates, such as the peaks at 728 cm^{-1} (C-C stretching, proline), 880 cm^{-1} (tryptophan, δ (ring)), 960 cm^{-1} (hydroxyapatite, carotenoid, and cholesterol), 1005 cm^{-1} (phenylalanine (proteins); proteins symmetric ring breathing of phenylalanine), 1079 cm^{-1} (C-C or C-O
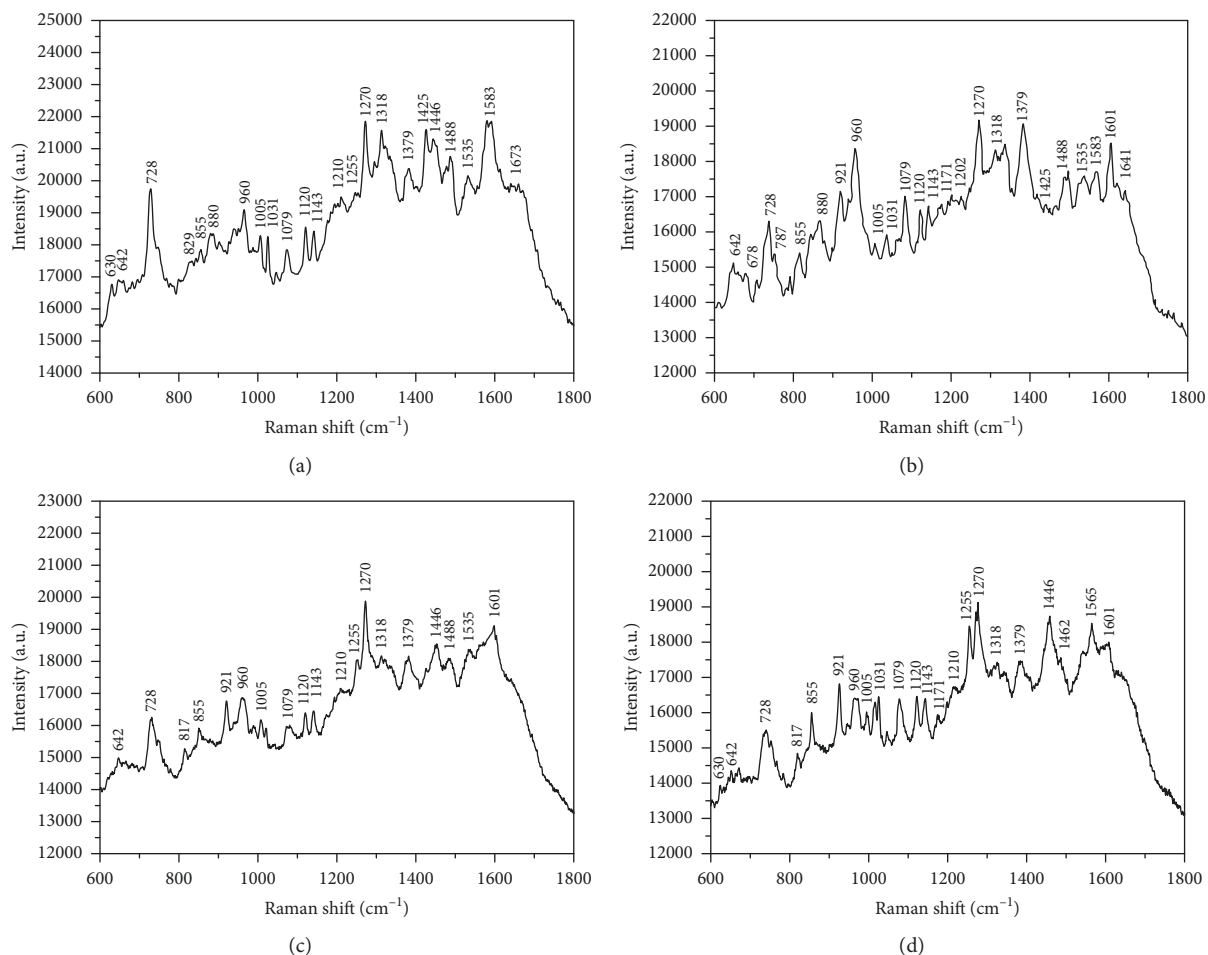
(a)

(b)

(c)

(d)

FIGURE 4: Average SERS spectra of serum obtained from (a) large cell lung cancer patients, (b) lung adenocarcinoma patients, (c) lung squamous carcinoma patients, and (d) healthy subjects.

stretching mode of phospholipids), 1120 cm^{-1} (the strong C-O band of ribose), 1171 cm^{-1} ((CH) phenylalanine, tyrosine), 1318 cm^{-1} (G ring breathing modes of the DNA/RNA), 1379 cm^{-1} (δCH$_3$ symmetric (lipid assignment)), 1446 cm^{-1} (CH$_2$ bending mode of proteins and lipids), and 1583 cm^{-1} (δ(C=C), phenylalanine). Although the different groups have similar SERS spectral profiles, such as peak positions and spectral bandwidths, some little differences can be observed. Then, in order to discriminate among different types of NSCLC, the differences between SERS spectra of four groups are compared, and the results with details are as follows:

For the convenient comparison, the intensity of average SERS spectrum for serum of each group was normalized to a range from 0 to 1 (Figure 5). The intensity of peak at 1270 cm^{-1} (typical phospholipids, C=C groups in fatty acids, amide III band in proteins) was the reference for normalization because of the narrow peak width, high intensity, and the nonsensitivity to environmental change. To better understand the SERS spectra differences, the difference spectra were computed, which can better interpret the spectral differences and gain insight into the biochemical variation. Thus, the difference spectra were computed by subtracting
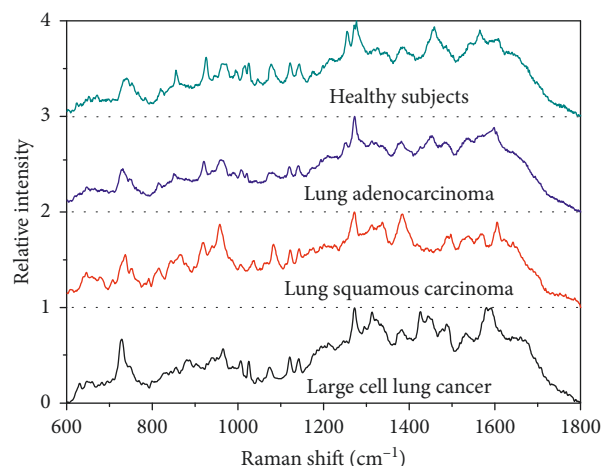

FIGURE 5: The normalized mean SERS spectra of serum obtained from (black curve) large cell lung cancer patients, (red curve) lung squamous carcinoma patients, (blue curve) lung adenocarcinoma patients, and (green curve) healthy subjects.

the spectrum of healthy subjects from the spectrum of large cell lung cancer (healthy subjects–large cell lung cancer), the spectrum of healthy subjects from the spectrum of lung

squamous carcinoma (healthy subjects–lung squamous carcinoma), the spectrum of healthy subjects from the spectrum of lung adenocarcinoma (healthy subjects–lung adenocarcinoma), the spectrum of lung adenocarcinoma from the spectrum of lung squamous carcinoma (lung adenocarcinoma–lung squamous carcinoma), the spectrum of lung adenocarcinoma from the spectrum of large cell lung cancer (lung adenocarcinoma–large cell lung cancer), and the spectrum of lung squamous carcinoma from the spectrum of large cell lung cancer (lung squamous carcinoma–large cell lung cancer). According to reference to the Raman peak assignments in Table 2, we could assign the characteristic peaks in six difference spectra.

As shown in Figure 6(a) (healthy subjects–large cell lung cancer), we could learn that the positive peaks at 855 cm^{-1} (proline, hydroxyproline, and tyrosine C-C stretching), 921 cm^{-1} (C-C stretch of proline ring/glucose/lactic acid; C-C, praline ring (collagen assignment)), 960 cm^{-1}, 1079 cm^{-1}, 1120 cm^{-1} (the strong C-O band of ribose), 1255 cm^{-1} (lipids), and 1565 cm^{-1} (tryptophan) were from the spectrum of healthy subjects, indicating the relative intensity of these peaks which were mainly the vibration bands of some amino acid and lipids were higher in the spectrum of serum obtained from healthy subjects when compared with that of large cell lung cancer patients, whereas the negative bands for Figure 6(a) at 642 cm^{-1} (C-C twisting mode of tyrosine), 728 cm^{-1}, 787 cm^{-1} (uracil-based ring breathing mode), 829 cm^{-1} (O-P-O stretching DNA/RNA; $\nu_2 PO_2^{2-}$ stretch of nucleic acids), 1005 cm^{-1}, 1181 cm^{-1}, 1318 cm^{-1}, 1379 cm^{-1}, 1425 cm^{-1} (G, A (DNA, RNA)), 1488 cm^{-1} (guanine (N$_7$)), 1583 cm^{-1}, and 1673 cm^{-1} (amide I) were from the spectrum of serum obtained from large cell lung cancer patients. These peaks were mainly generated by the vibration peaks of DNA, RNA, and proteins. In Figure 6(b) (healthy subjects–lung squamous carcinoma), the positive bands at 1017 cm^{-1} (carbohydrates peak), 1255 cm^{-1} (lipids), 1446 cm^{-1}, 1565 cm^{-1}, and 1673 cm^{-1} were from healthy subjects. The majority of these peaks could be assigned to carbohydrates and lipids. The negative bands, 642 cm^{-1}, 728 cm^{-1}, 880 cm^{-1}, 960 cm^{-1}, 1031 cm^{-1}, 1379 cm^{-1}, 1488 cm^{-1}, and 1601 cm^{-1} (amide I band of proteins) from the spectrum of lung squamous carcinoma and could be similarly assigned as nucleic acid and proteins. In Figure 6(c), compared with the lung adenocarcinoma, the intensities of healthy subjects at 855 cm^{-1}, 921 cm^{-1}, 1031 cm^{-1}, 1079 cm^{-1}, 1120 cm^{-1}, 1255 cm^{-1}, 1446 cm^{-1}, 1565 cm^{-1}, and 1673 cm^{-1} increased, which were assigned to the molecular structures in the amino acid and lipids, but the intensities of peaks at 642 cm^{-1}, 728 cm^{-1}, 817 cm^{-1} (C-C stretching (protein)), 960 cm^{-1}, 1425 cm^{-1}, 1534 cm^{-1} (amide carbonyl group vibrations and aromatic hydrogens), and 1583 cm^{-1} decreased, which were mainly assigned to the relative molecular structures of nucleic acids and protein. The distinctive SERS features and intensity differences for NSCLC and normal serum could reflect their molecular changes in quantity or structure.

Furthermore, we compared the differences among the spectrum of serum obtained from three type of NSCLC. As shown in Figure 6(d) (lung adenocarcinoma–lung squamous

TABLE 2: Peak assignments for SERS spectra of serum.

Raman shift (cm^{-1})	Peak assignment
630	Glycerol
642	C-C twisting mode of tyrosine
678	Ring breathing modes in the DNA bases
728	C-C stretching, proline
787	Uracil-based ring breathing mode
817	C-C stretching (protein)
829	O-P-O stretching DNA/RNA; $\nu_2 PO_2^{2-}$ stretch of nucleic acids
855	Proline, hydroxyproline, and tyrosine C-C stretching
880	Tryptophan, δ (ring)
921	C-C stretch of proline ring/glucose/lactic acid; C-C, praline ring (collagen assignment)
960	Hydroxyapatite, carotenoid, and cholesterol
1005	Phenylalanine (proteins); proteins symmetric ring breathing of phenylalanine
1017	Carbohydrates peak
1031	Phenylalanine, C-N stretching of proteins; C-H in-plane bending mode of phenylalanine
1047	Glycogen
1079	C-C or C-O stretching mode of phospholipids
1120	The strong C-O band of ribose
1143	C-O stretching (carbohydrates)
1171	Tyrosine; (CH) phenylalanine, tyrosine
1210	C-C$_6$H$_5$ stretching mode in tyrosine and phenylalanine
1255	Lipids
1270	Typical phospholipids, C=C groups in fatty acids, amide III band in proteins
1318	G (ring breathing modes of the DNA/RNA bases)
1335	Polynucleotide chain (DNA purine bases)
1379	δCH_3 symmetric (lipid assignment)
1425	G, A (DNA, RNA)
1446	CH$_2$ bending mode of proteins and lipids; CH$_2$ deformation
1462	δCH_2, disaccharides
1488	Guanine (N$_7$)
1534	Amide carbonyl group vibrations and aromatic hydrogens
1565	Tryptophan
1583	C=C bending mode of phenylalanine
1601	Amide I band of proteins
1641	Amide I band (protein band)
1673	Amide I

Raman peaks assignments are based on Ref. [25–37].

carcinoma), the positive bands at 630 cm^{-1} (glycerol), 1446 cm^{-1}, 1583 cm^{-1}, and 1673 cm^{-1} were due to the spectrum of lung adenocarcinoma. In contrast, the negative bands at 642 cm^{-1}, 728 cm^{-1}, 787 cm^{-1}, 880 cm^{-1}, 960 cm^{-1}, 1031 cm^{-1}, 1079 cm^{-1}, 1171 cm^{-1}, 1335 cm^{-1} (Polynucleotide chain (DNA purine bases)), and 1379 cm^{-1} (δCH_3 symmetric (lipid assignment)) were due to the spectrum of lung squamous carcinoma. Figure 6(e) (lung adenocarcinoma–large cell lung cancer) showed the positive bands at 642 cm^{-1}, 678 cm^{-1} (ring breathing modes in the DNA bases), 817 cm^{-1} (C-C stretching (protein)), 921 cm^{-1}, 960 cm^{-1}, 1079 cm^{-1}, and 1601 cm^{-1} were from the spectrum of lung adenocarcinoma, whereas the negative bands at

(a)

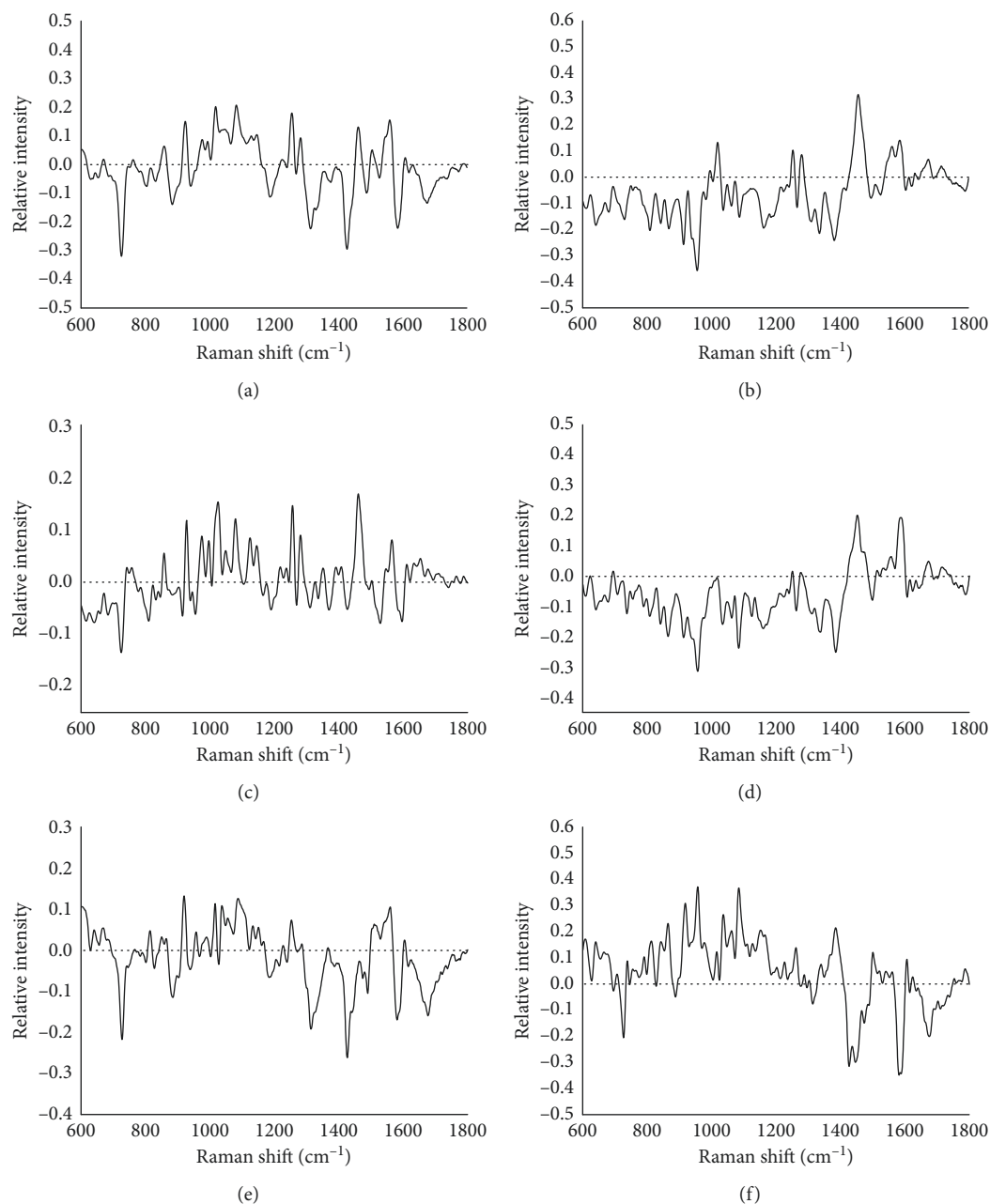

(b)

(c)

(d)

(e)

(f)

FIGURE 6: Difference spectra among the four groups were computed: (a) healthy subjects–large cell lung cancer, (b) healthy subjects–lung squamous carcinoma, (c) healthy subjects–lung adenocarcinoma, (d) lung adenocarcinoma–lung squamous carcinoma, (e) lung adenocarcinoma–large cell lung cancer, and (f) lung squamous carcinoma–large cell lung cancer.

$728\,cm^{-1}$, $880\,cm^{-1}$, $1031\,cm^{-1}$, $1171\,cm^{-1}$, $1210\,cm^{-1}$ (C-C_6H_5 stretching mode in tyrosine and phenylalanine), $1318\,cm^{-1}$, $1425\,cm^{-1}$, $1583\,cm^{-1}$, and $1673\,cm^{-1}$ were from large cell lung cancer. The different spectrum from lung squamous carcinoma and large cell lung cancer showed the positive bands at $642\,cm^{-1}$, $787\,cm^{-1}$, $817\,cm^{-1}$, $855\,cm^{-1}$, $960\,cm^{-1}$, $1031\,cm^{-1}$, $1079\,cm^{-1}$, $1171\,cm^{-1}$, $1255\,cm^{-1}$, $1379\,cm^{-1}$, and $1601\,cm^{-1}$, and the negative bands at $728\,cm^{-1}$, $880\,cm^{-1}$, $1318\,cm^{-1}$, $1425\,cm^{-1}$, $1446\,cm^{-1}$, $1583\,cm^{-1}$, and $1673\,cm^{-1}$ (Figure 6(f)). These peaks have been previously assigned in Table 2. The above results indicated that the serum from healthy subjects have less

nucleic acids and proteins than those of NSCLC patients, which could be resulting from the abnormal metabolism of nucleic acids and proteins in the patients. The cell-free nucleic acids are significantly increased, which originated from the regeneration, necrosis, and release of intact cells in the bloodstream and their subsequent lysis. This result was consistent with the previous reports [38]. Beyond that, the amounts of some amino acids and lipids in the serums from the healthy subjects were more than those of NSCLC patients. Meanwhile, there are also differences among the spectrums of serum obtained from three different types of NSCLC, including the bands at $728\,cm^{-1}$, $880\,cm^{-1}$,
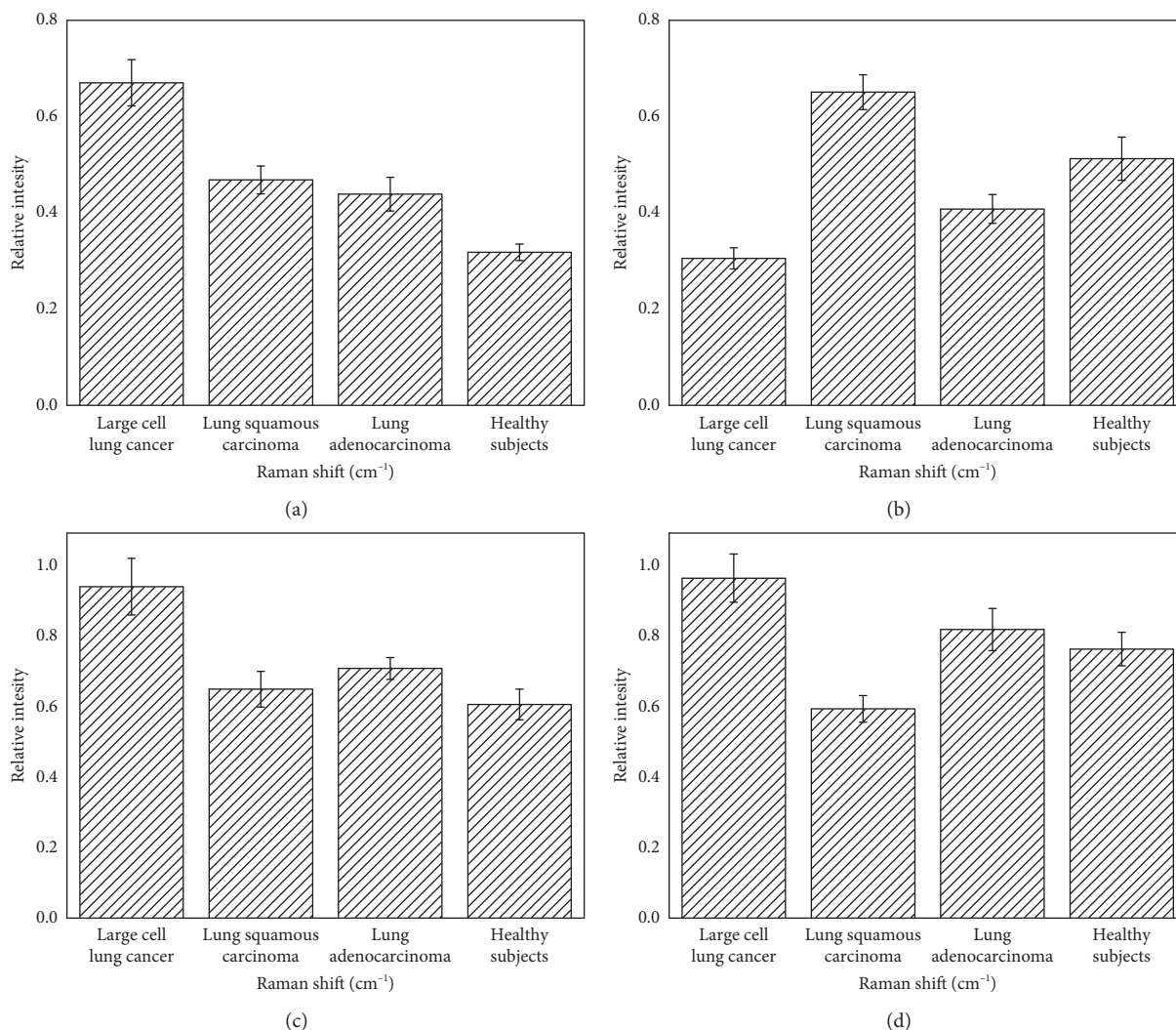
FIGURE 7: The comparison of mean relative intensity at (a) $728\,cm^{-1}$, (b) $1079\,cm^{-1}$, (c) $1318\,cm^{-1}$, and (d) $1466\,cm^{-1}$ among four groups.

$921\,cm^{-1}$, $960\,cm^{-1}$, $1318\,cm^{-1}$, $1446\,cm^{-1}$, $1583\,cm^{-1}$, and so on.

To further quantify the differences among the four groups based on the normalized mean SERS spectra of each NSCLC type, we compared the mean relative intensity at four different Raman peaks, including $728\,cm^{-1}$, $1079\,cm^{-1}$, $1318\,cm^{-1}$, and $1466\,cm^{-1}$. From Figure 7, healthy subjects showed higher relative intensity of Raman peaks at $1079\,cm^{-1}$ and $1466\,cm^{-1}$ than the three types of NSCLC. However, compared with healthy subjects, the relative intensity of Raman peaks at $728\,cm^{-1}$ and $1318\,cm^{-1}$ for three types of NSCLC is higher. Furthermore, there are also many differences among the three types of NSCLC. As to the relative intensity of Raman peaks at $728\,cm^{-1}$ and $1318\,cm^{-1}$, large cell lung cancer was higher than lung squamous carcinoma and lung adenocarcinoma. The relative intensity of Raman peak at $1079\,cm^{-1}$ for lung squamous carcinoma was significantly higher than others, and there was no significance at $1466\,cm^{-1}$ among the three types of NSCLC. Based on the above analysis, we could learn that the result is consistent with difference spectra analysis.

3.4. PCA Analysis. In order to determine if SERS spectroscopy could be used to distinguish the different types of NSCLC, principal component analysis (PCA) was applied. PCA is a multivariate method widely used in spectral analysis, which defines a new dimensional space in which the major variance in the original dataset can be captured and represented by only a few principal component (PC) variables. Scores of PCs are one of the parameters widely used for classification [39]. In Figure 8, using principal component scores PC1 (66.7% variation) and PC2 (15.2% variation), the scatter plots of SERS spectra for each type of NSCLC about twenty subjects were projected into the two-dimensional images, which could be used to classify the types of NSCLC. In the PCA score plot, the data points of healthy subjects and three types of NSCLC are clustered into four separate groups. The plots group of healthy subjects was clearly separable from the groups of large cell lung cancer, lung squamous carcinoma group, and lung adenocarcinoma group because of the differences in serum composition obtained from healthy subjects and NSCLC patients. Three kinds of cancer groups have more nucleic acids and proteins,
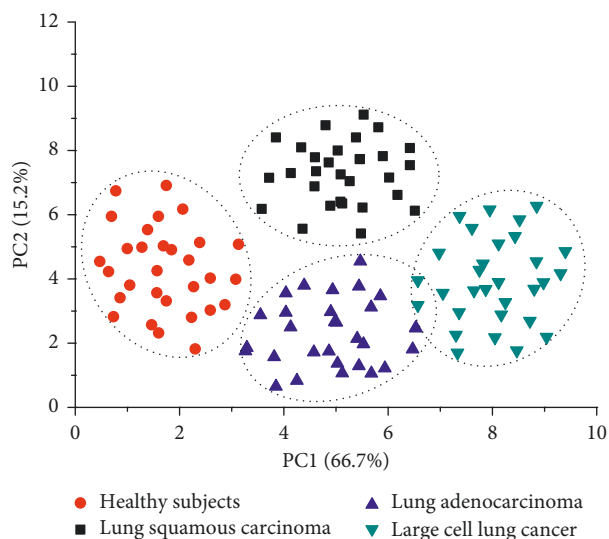
FIGURE 8: PCA score plots of SERS spectra for serum obtained from large cell lung cancer patients, lung squamous carcinoma patients, lung adenocarcinoma patients, and healthy subjects. Each type of NSCLC was coded with a different color.

but have less amino acids and lipids than healthy subjects. However, the plots group of lung adenocarcinoma are adjacent to the lung squamous carcinoma groups and have a small overlap with the large cell lung cancer groups. This was mainly due to similar biochemical composition among NSCLC. PCA gives more intuitive results than direct analysis spectral difference among different types of NSCLC. The results suggest that PCA can easily classify the types of NSCLC based on their specific spectral features.

4. Conclusions

The serum samples are easily collected in clinical examination, and mostly reflect some vital subtle change caused by tumors in the metabolism environment, such as amino acid metabolism, miRNA expression, and biomarkers generation. The concentration of nucleic acids and the composition of proteins from the serum samples of NSCLC patients are different from the normal samples, which are believed to originate from apoptosis, tumor necrosis, and associated metabolites. Therefore, serum detection is appropriate for NSCLC diagnosis.

In our study, the SERS diagnostic approach was explored in terms of its ability to discriminate the NSCLC types based on HGNP substrates. HGNPs were synthesized by a simple, fast, and large-scale method. Via electrostatic action, HGNPs were assembled on the surface of a silicon wafer, and these substrates exhibited very good reproducibility, homogeneous SERS activity, and a high SERS enhancement effect. HGNP substrates enabled us to successfully detect the SERS spectra of serum obtained from healthy subjects and three different types of NSCLC patients (lung adenocarcinoma, lung squamous carcinoma, and large cell lung cancer). The different spectra analysis showed that there were differences in the intensity and position of SERS peaks assigned to various biochemical changes in the serum among

the four groups. Compared with the SERS spectra of the normal serum, serum obtained from NSCLC have more nucleic acids and proteins, but have less amino acids and lipids. There are also significant differences in the biochemical components among the three different types of NSCLC. The SERS of human serum combined with PCA achieved a successful segregation of different types of NSCLC. This exploratory work demonstrates that SERS serum analysis technique has potential for improving NSCLC detection and screening.

Data Availability

The data used to support the findings of this study are available from the corresponding author upon request.

Conflicts of Interest

The authors declare that they have no conflicts of interest.

Acknowledgments

References

[1] B. Haaland, P. S. Tan, G. J. de Castro, and G. Lopes, "Meta-analysis of first-line therapies in advanced non-small-cell lung cancer harboring EGFR-activating mutations," *Journal of Thoracic Oncology*, vol. 9, no. 6, pp. 805–811, 2014.

[2] H. Asamura, T. Goya, Y. Koshiishi et al., "A Japanese lung cancer registry study: prognosis of 13,010 resected lung cancers," *Journal of Thoracic Oncology*, vol. 3, no. 1, pp. 46–52, 2008.

[3] C. H. Dai, J. Li, L. C. Yu, X. Q. Li, S. B. Shi, and J. R. Wu, "Molecular diagnosis and prognostic significance of lymph node micrometastasis in patients with histologically node-negative non-small cell lung cancer," *Tumor Biology*, vol. 34, no. 2, pp. 1245–1253, 2013.

[4] M. Bonomi, S. Pilotto, M. Milella et al., "Adjuvant chemotherapy for resected non-small-cell lung cancer: future perspectives for clinical research," *Journal of Experimental and Clinical Cancer Research*, vol. 30, no. 1, pp. 115–122, 2011.

[5] D. P. Lau, Z. Huang, H. Liu et al., "Raman spectroscopy for optical diagnosis in normal and cancerous tissue of the nasopharynx? Preliminary findings," *Laser in Surgery and Medicine*, vol. 32, no. 3, pp. 210–214, 2003.

[6] J. H. Kim, W. W. Bryan, and T. R. Lee, "Preparation, characterization, and optical properties of gold, silver, and Gold–Silver alloy nanoshells having silica cores," *Langmuir*, vol. 24, no. 19, pp. 11147–11152, 2008.

[7] M. Sanles-Sobrido, W. Exner, L. Rodriguez-Lorenzo et al., "Design of SERS-encoded, submicron, hollow particles through confined growth of encapsulated metal nanoparticles," *Journal of the American Chemical Society*, vol. 131, no. 7, pp. 2699–2705, 2009.

[8] K. A. Willets, "Surface-enhanced Raman scattering (SERS) for probing internal cellular structure and dynamics," *Analytical and Bioanalytical Chemistry*, vol. 394, no. 1, pp. 85–94, 2009.

[9] J. Q. Lin, J. Wang, C. X. Xu et al., "Differentiation of digestive system cancers by using serum protein-based surface-enhanced Raman spectroscopy," *Journal of Raman Spectroscopy*, vol. 48, no. 1, pp. 16–21, 2017.

[10] B. Yan, B. Li, Z. N. Wen, X. Y. Luo, L. L. Xue, and L. J. Li, "Label-free blood serum detection by using surface-enhanced Raman spectroscopy and support vector machine for the preoperative diagnosis of parotid gland tumors," *BMC Cancer*, vol. 15, no. 1, p. 650, 2015.

[11] S. Feng, R. Chen, J. Lin et al., "Gastric cancer detection based on blood plasma surface-enhanced Raman spectroscopy excited by polarized laser light," *Biosensor and Bioelectronics*, vol. 26, no. 7, pp. 3167–3174, 2011.

[12] X. Z. Li, T. Y. Yang, S. Q. Li, D. L. Wang, Y. T. Song, and K. D. Yu, "Different classification algorithms and serum surface enhanced Raman spectroscopy for noninvasive discrimination of gastric diseases," *Journal of Raman Spectroscopy*, vol. 47, no. 8, pp. 917–925, 2016.

[13] J. L. González-Solís, J. C. Martínez-Espinosa, J. M. Salgado-Román, and P. Palomares-Anda, "Monitoring of chemotherapy leukemia treatment using Raman spectroscopy and principal component analysis," *Lasers in Medical Science*, vol. 29, no. 3, pp. 1241–1249, 2014.

[14] L. C. Kennedy, L. R. Bickford, N. A. Lewinski et al., "A new era for cancer treatment: gold-nanoparticle-mediated thermal therapies," *Small*, vol. 7, no. 2, pp. 169–183, 2011.

[15] Y. Lu, Y. Yin, Z. Y. Li, and Y. Xia, "Colloidal crystals made of polystyrene spheroids: fabrication and structural/optical characterization," *Langmuir*, vol. 18, no. 20, pp. 7722–7727, 2002.

[16] E. Hao, S. Li, R. C. Bailey, S. Zou, G. C. Schatz, and J. T. Hupp, "Optical properties of metal nanoshells," *Journal of Physical Chemistry B*, vol. 108, no. 4, pp. 1224–1229, 2004.

[17] C. Y. Song, N. Zhou, B. Y. Yang, Y. J. Yang, and L. H. Wang, "Facile synthesis of hydrangea flower-like hierarchical gold nanostructures with tunable surface topographies for single-particle surface-enhanced Raman scattering," *Nanoscale*, vol. 7, no. 40, pp. 17004–17011, 2015.

[18] L. Rodríguez-Lorenzo, Z. Krpetic, S. Barbosa et al., "Intracellular mapping with SERS-encoded gold nanostars," *Integrative Biology*, vol. 3, no. 9, pp. 922–926, 2011.

[19] X. Wang, X. M. Qian, J. J. Beitler et al., "Detection of circulating tumor cells in human peripheral blood using surface-enhanced Raman scattering nanoparticles," *Cancer Research*, vol. 71, no. 5, pp. 1526–1532, 2011.

[20] L. Rodrı´guez-Lorenzo, R. A. A´lvarez-Puebla, I. Pastoriza-Santos et al., "Zeptomol detection through controlled ultrasensitive surface-enhanced Raman scattering," *Journal of the American Chemical Society*, vol. 131, no. 13, pp. 4616–4618, 2009.

[21] A. S. D. S. Indrasekara, S. Meyers, S. Shubeita, L. C. Feldman, T. Gustafssonc, and L. Fabris, "Gold nanostar substrates for SERS-based chemical sensing in the femtomolar regime," *Nanoscale*, vol. 6, no. 15, pp. 8889–8899, 2014.

[22] C. E. Talley, L. Jusinski, C. W. Hollars, S. M. Lane, and T. Huser, "Intracellular pH sensors based on surface-enhanced Raman scattering," *Analytical Chemistry*, vol. 76, no. 23, pp. 7064–7068, 2005.

[23] E. Nalbant Esenturk and A. R. HightWalker, "Surface-enhanced Raman scattering spectroscopy via gold nanostars," *Journal of Raman Spectroscopy*, vol. 40, no. 1, pp. 86–91, 2009.

[24] M. Zhu, M. Z. Lerum, and W. Chen, "How to prepare reproducible, homogeneous, and hydrolytically stable aminosilane-derived layers on silica," *Langmuir*, vol. 28, no. 1, pp. 416–423, 2012.

[25] C. J. Frank, R. L. McCreecy, and D. C. B. Redd, "Raman spectroscopy of normal and diseased human breast tissues," *Analytical Chemistry*, vol. 67, no. 5, pp. 777–783, 1995.

[26] G. Shetty, C. Kedall, N. Shepherd, N. Stone, and H. Barr, "Raman spectroscopy: elucidation of biochemical changes in carcinogenesis of oesophagu," *British Journal of Cancer*, vol. 94, no. 10, pp. 1460–1464, 2006.

[27] N. Stone, C. Kendall, J. Smith, P. Crow, and H. Barr, "Raman spectroscopy for identification of epithelial cancers," *Faraday Discussion*, vol. 126, pp. 141–157, 2004.

[28] I. Notingher, C. Green, C. Dyer et al., "Discrimination between ricin and sulphur mustard toxicity in vitro using Raman spectroscopy," *Journal of the Royal Society Interface*, vol. 1, no. 1, pp. 79–90, 2004.

[29] Z. Huang, A. McWilliams, M. Lui, D. I. McLean, S. Lam, and H. Zeng, "Near-infrared Raman spectroscopy for optical diagnosis of lung cancer," *International Journal of Cancer*, vol. 107, no. 6, pp. 1047–1052, 2003.

[30] B. Swinson, W. Jerjes, M. El-Maaytah, P. Norris, and C. Hopper, "Optical techniques in diagnosis of head and neck malignancy," *Oral Oncology*, vol. 42, no. 3, pp. 221–228, 2006.

[31] R. Jyothi Lakshmi, V. B. Kartha, C. M. Krishna, J. G. R. Solomon, G. Ullas, and P. Uma Devi, "Tissue Raman spectroscopy for the study of radiation damage: brain irradiation of mice," *Radiation Research*, vol. 157, no. 2, pp. 175–182, 2002.

[32] C. Krafft, L. Neudert, T. Simat, and R. Salzer, "Near infrared Raman spectra of human brain lipids," *Spectrochimica Acta. Part A, Molecular and Bimolecular Spectroscopy*, vol. 61, no. 7, pp. 1529–1535, 2005.

[33] J. W. Chan, D. S. Taylor, T. Zwerdling, S. T. Lane, K. Ihara, and T. Huser, "Micro-Raman spectroscopy detects individual neoplastic and normal hematopoietic cells," *Biophysical Journal*, vol. 90, no. 2, pp. 648–656, 2006.

[34] E. Kateinen, M. Elomaa, U. M. Laakkonen et al., "Qualification of the amphetamine content in seized street samples by Raman spectroscopy," *Forensic Science International*, vol. 52, no. 1, pp. 88–92, 2007.

[35] E. O. Faolain, M. B. Hunter, J. M. Byrne et al., "A study examining the effects of tissue processing on human tissue sections using vibrational spectroscopy," *Vibrational Spectroscopy*, vol. 38, no. 1-2, pp. 121–127, 2005.

[36] A. J. Ruiz-Chica, M. A. Medina, F. Sanchez-Jimenez, and F. J. Ramirez, "Characterization by Raman spectroscopy of conformational changes on guaninecytosine and adeninethymine oligonucleotides induced by aminooxy analogues of spermidine," *Journal of Raman Spectroscopy*, vol. 35, no. 2, pp. 93–100, 2004.

[37] B. R. Wood, M. A. Quinn, B. Tait et al., "FTIR microspectroscopic study of cell types and potential confounding variables in screening for cervical malignancies," *Biospectroscopy*, vol. 4, no. 2, pp. 75–91, 1998.

[38] S. Y. Feng, R. Chen, J. Q. Lin et al., "Nasopharyngeal cancer detection based on blood plasma surface-enhanced Raman spectroscopy and multivariate analysis," *Biosensor and Bioelectronics*, vol. 25, no. 11, pp. 2414–2419, 2010.

[39] S. Y. Feng, J. Q. Lin, M. Cheng et al., "Blood plasma surface-enhanced Raman spectroscopy for non-invasive optical detection of cervical cancer," *Analyst*, vol. 138, no. 14, pp. 3967–3974, 2013.